LANGMUIR

Article

Effects of Strain and Kinetics on the H$_2$O$_2$-Assisted Reconstruction of Ag−Au−Ag Nanorods

Hui Hao, Yinliang Yang, Chao Zou, Wei Chen, Haihong Wen,* Wei Wang,* and Yun Yang*

Cite This: *Langmuir* 2020, 36, 9770−9779

Read Online

ACCESS | Metrics & More | Article Recommendations | Supporting Information

ABSTRACT: Morphology of Ag nanocrystals (NCs) is essential to the NC application in catalysis, optics, and as antibacterial agents. Therefore, it is important to develop synthetic methods and understand the evaluation of NC morphology in different chemical environments. In this study, we report interesting findings of the morphological change of fivefold-twinned Ag−Au−Ag nanorods (NRs) under the effect of H$_2$O$_2$ both as an oxidant (etchant) and a reductant. At low H$_2$O$_2$ concentration, the reconstruction of Ag−Au−Ag NRs was dominated by the growth along the longitudinal direction of NRs. With the increase of H$_2$O$_2$ concentration, the reconstruction also occurs in the transverse direction, and a clear change in particle morphology was observed. We further systematically studied the mechanism of the reaction. The results showed that the transition of the morphology was a two-step process: (1) the etching of Ag on the seeds and (2) the reduction of Ag$_2$O. In the second step, the reaction kinetics was highly affected by H$_2$O$_2$ concentration. At low H$_2$O$_2$ concentration, the growth mainly occurs along ⟨110⟩. However, at high H$_2$O$_2$ concentration, the reduction of Ag was not facet-selective. Using the developed method, we can prepare various bimetallic NCs (high aspect ratio NRs with abundant pinholes, nanoplates, and other NCs). The effect of the reconstruction process on the surface-enhanced Raman scattering (SERS) performance of NCs was investigated.
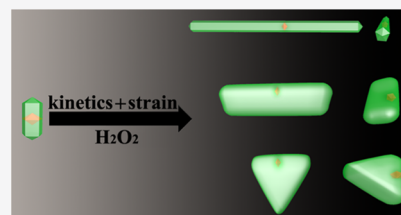
INTRODUCTION

Noble nanocrystals (NCs) attracted much attention in the past few decades due to their potential applications in cancer therapy, catalysis, optics, and electronics.[1−5] Among noble NCs, Ag−Au bimetallic NCs have excellent optical performances because both metals have fine-tuned localized surface plasmon resonance absorption in the visible and near-infrared region.[6−10] The structure and composition of Ag−Au bimetallic NCs strongly affect their physical and chemical properties.[11−17] Therefore, the development of new methods and technology for controllably preparing Ag−Au bimetallic NCs is of great interest in both fundamental research of crystal growth and meeting the needs of practical applications.

For the controlled preparations of Ag−Au bimetallic NCs, various technologies (seed-mediated growth, soft template, thermo-decomposition, and etching) have been demonstrated to be effective.[18−25] Of them, etching is a very powerful tool to tune the morphology, composition, and structure of NCs. For example, galvanic etching can be used to synthesize diverse hollow nanostructures.[26−30] Other chemical etchings were also adopted in many reports and O$_2$ in the air often serves as an etchant.[31,32] Compared to O$_2$, H$_2$O$_2$ possesses stronger etching capacity and can oxidize some noble metals, especially Ag.[31] Thereby, H$_2$O$_2$ is very popular in the rapid construction of Ag NCs. Yang's group prepared a variety of multibranched Ag NCs by suffering Ag octahedral NCs to position-specific etching in H$_2$O$_2$ and aqua ammonia.[31] The oxidation capacity of H$_2$O$_2$ has been a scientific fact for a very long time. Interestingly, several reports showed that H$_2$O$_2$ could trigger the shape transformation of Ag NCs from a sphere to a plate.[33−35] In these studies, the mechanism that H$_2$O$_2$ may serve as an oxidant to oxidize Ag nanospheres to Ag(I) and then as a reductant to transform Ag(I) to Ag atoms for growing nanoplates was proposed. The studies also demonstrated that this strategy had a size limit. The shape transformation cannot be achieved when the diameter of starting Ag nanospheres is larger than 10 nm. Moreover, such H$_2$O$_2$-triggered shape transformation has not been fully understood so far, and a lot of questions remain unanswered. For example, is this technology only suitable for synthesizing platelike Ag NCs? Can other shaped Ag NCs be used as starting materials? Therefore, it is worth putting more efforts to explore this technology, and only by doing so, the mechanism could be fully understood based on solid scientific evidence. Here, we adopted large-sized Ag−Au−Ag segmental nanorods (NRs) as starting materials and found that the method is still very effective compared to bimetallic nonspherical NCs and challenging the above size limit. A variety of bimetallic NCs, including high aspect ratio NRs and nanoplates, were prepared by adjusting the kinetics of crystal growth. The prepared long
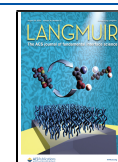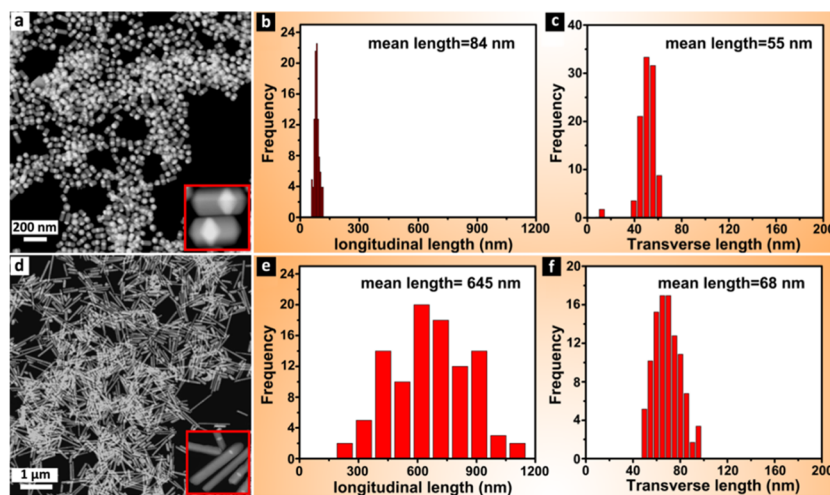
Figure 1. HAADF images and length distribution histograms of short Ag−Au−Ag NRs untreated with H_2O_2 (a−c) and long Ag−Au−Ag NRs after treated with H_2O_2 (d−f). Insets in (a) and (d) are the high-magnification HAADF images.

Ag−Au−Ag NRs have abundant pinholes on their surface, and therefore exhibit better surface-enhanced Raman scattering (SERS) performance.

MATERIALS AND METHODS

Materials. Chloroauric acid ($HAuCl_4·4H_2O$) was purchased from Shanghai Chemical Ltd. Silver nitrate ($AgNO_3$) was purchased from Sinopharm Group Co. Ltd. Poly(diallyldimethylammonium chloride) (PDDA) with molecular weight 400 000−500 000, hydrogen peroxide (H_2O_2), sodium chloride (NaCl), sodium hydroxide (NaOH), and ammonium hydroxide (NH_4OH, 20 wt % in water) were purchased from Shanghai Aladdin Reagent Co. Ltd. Diethylene glycol (DEG) was purchased from Xilong Chemicals Co. Ltd. 2-Naphthalenethiol was purchased from Sigma-Aldrich. All chemicals were of analytical grade and used as received. Deionized water (18.2 MΩ cm) was obtained using Elix-Milli-Q (Millipore) and used in all experiments.

Preparations of Au Decahedral NCs and Segmental Ag−Au−Ag NRs. Au decahedral NCs and segmental Ag−Au−Ag NRs were prepared by following the methods reported previously.[36,37] First, a DEG solution containing $AgNO_3$ was prepared with a concentration of 10 mg/mL. Then, PDDA (60 μL) was mixed with 10 mL of DEG, 12.5 μL of $HAuCl_4$ (0.48 mol/L), and 600 μL of $AgNO_3$ DEG solution. The solution was well mixed at room temperature and then heated in a 210 °C oil bath. In about 15 min, the solution turned red, indicating the formation of Au decahedral NCs. After 30 min, the solution was cooled to room temperature and then 10.6 mL of water was introduced. For the synthesis of segmental Ag−Au−Ag NRs, an AgCl suspension was first prepared by mixing 5 mL of NaCl aqueous solution (2.8 mg/mL) with 5 mL of $AgNO_3$ aqueous solution (8 mg/mL). Then, 1.5 mL of NH_4OH was added to the AgCl suspension. The mixture immediately became transparent due to the formation of water-soluble $[Ag(NH_3)_2]^+$. Then, 20 mL of Au decahedral NC solution was mixed with 700 μL of $[Ag(NH_3)_2]^+$ solution. The mixtures were warmed up to 70 °C and stirred for 12 h for growing Ag−Au−Ag NRs. For purification, 1 mL of Ag−Au−Ag NR solution was mixed with 8 mL of water and then the NRs were precipitated through centrifugation. The above process was repeated three times to remove excess PDDA, DEG, and other by-products. The resulting precipitate was dispersed in 2 mL of deionized water.

Reconstruction of Ag/Au NCs. The purified Ag−Au−Ag NR solution (2 mL) was mixed with different volumes of H_2O_2 (0.03 wt % in water) in a 10 mL plastic tube and followed by 5 min ultrasonic treatment. Then, the mixture was allowed to stand without disturbance at room temperature. After 24 h, the supernatant liquid was taken out carefully using a plastic dropper and discarded, and then the precipitates were dispersed in 1 mL of water. Because no organics were added, further purification was not needed.

SERS Measurement. Ethanol solution of 2-naphthalenethiol (2 × 10^{-5} mol/L, 0.5 mL) was mixed with 0.5 mL of water containing purified NCs (2.00 μmol of the metal in each case), followed by 30 min ultrasonic treatment. A capillary tube was filled with the above solution by imbibition and then was used to obtain Raman spectra on a Renishaw Ramascope micro-Raman system attached with a Leica microscope (a 50× objective was used). The excitation wavelength of the laser was 532 nm, in conjunction with a grating of 1200 lines/mm, at a power of 50% of the laser output.

Characterizations. An ultrahigh-resolution field-emission scanning electron microscope (SEM) (Nova 100, FEI) was used to observe the morphology of the NCs. Transmission electron microscopy (TEM) and high-resolution transmission electron microscopy (HRTEM) were carried out on a JEM-2100F microscope (JOEL, Japan) attached with a high-angle annular dark-field (HAADF) detector.

RESULTS AND DISCUSSION

Evolution from Short NRs to Long NRs. We used the short Ag−Au−Ag NRs (Figure 1a) as a starting material to study the morphological evolution. The synthetic method for the short Ag−Au−Ag NRs was previously reported by our group.[37] Due to the large difference between the atomic number of Ag (47) and Au (79), the HAADF image shows a clear segmental structure (Figure 1a). The white and gray sections are attributed to the Au atoms of decahedral NCs and Ag atoms, respectively. These PDDA-stabilized Ag−Au−Ag NRs can be dispersed in solvents with high polarity. After removing excess DEG, PDDA, and other by-products, the purified NRs were dispersed into water. To induce reconstruction, 150 μL of H_2O_2 was added into the above solution containing starting Ag−Au−Ag NRs, and then the solution was subjected to ultrasonic treatment, followed by 24 h structure reformation at room temperature. Some gray precipitates were observed at the bottom of the containers and the HAADF image shows that they are high aspect ratio NRs (Figure 1d). Their image contains one white section overlapped by the gray section, as well as starting Ag−Au−Ag NRs. The white section should be Au decahedral NCs because H_2O_2 is unable to etch Au at room temperature (Figure 1a). For the gray section, it is possible to be a substance containing Ag. The results of elemental mapping demonstrate this conclusion (Figure 2). The element distribution of Ag and Au agrees well with HAADF results
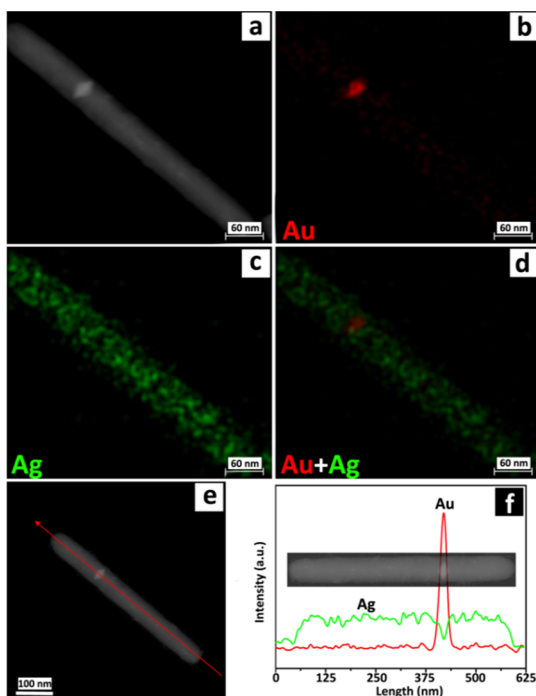
Figure 2. HAADF images (a), elemental mapping images (b−d), and elemental line scanning patterns (e, f) of one individual long Ag−Au−Ag NR. The red arrow in (e) indicates the scanning direction.

(Figure 2b−d). Elemental line scanning gives the same result (Figure 2e,f). These long NRs are indeed segmental Ag−Au−Ag NCs. This was confirmed by HRTEM images. Distinctly, the lattice fringe image in one NR demonstrates that it is highly crystalline (Figure 3a,b). The adjacent interplanar spacing is 0.238 nm attributable to Ag(111) (Figure 3c),[38] which demonstrates that the NR is composed of Ag atoms rather than the Ag(I)-related substance. The fast-Fourier transform (FFT) pattern manifests that the NR has no
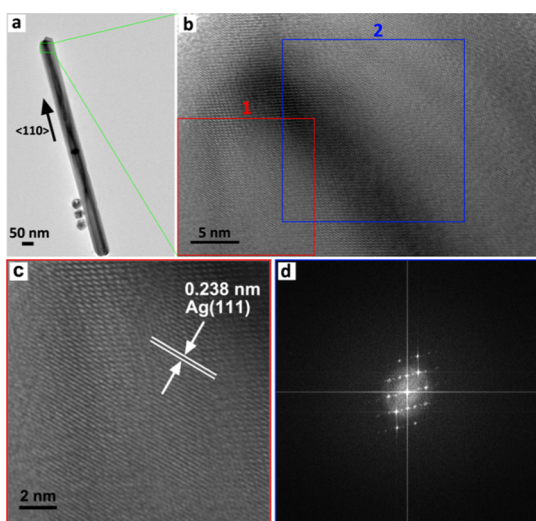

Figure 3. HRTEM images of one individual long Ag−Au−Ag NR (a) and a detailed HRTEM result (b) of the area marked by the green box in (a). (c) The detailed structure from the positions marked by the red box and (d) is the FFT pattern obtained based on the HRTEM result marked by the blue box in (b).

structure difference (Figure 3d), compared with the starting Ag−Au−Ag NRs, that is, both of them are fivefold-twinned.[39]

Although both NRs have the same structural features, their lengths are dramatically different. The starting Ag−Au−Ag NRs have a mean longitudinal length of 84 nm and a transverse length of 55 nm (Figure 1b,c). After the treatment with H_2O_2, the mean longitudinal length increased to 645 nm, and even some micron-sized NRs were observed (Figure 1e). However, their transverse length had no such significant change and only slightly increased by 13 nm (from 55 to 68 nm).

Effect of H_2O_2. In the results shown above, we observed the morphological transition of NRs from a low aspect ratio to a high aspect ratio by the treatment of H_2O_2, which motivates us to analyze the mechanism of the morphological transition. The system contains H_2O, PDDA, H_2O_2, Ag, and Au. H_2O often serves as a high-stability solvent in the synthesis of Ag NCs, and therefore, it is impossible to induce the size change to such an extent. Excess PDDA molecules have been removed during purification. Moreover, it has been reported that PDDA could act as a capping agent for preparing Ag−Au−Ag NRs and no such length change was observed.[37] Therefore, H_2O_2 is the only cause for the morphological transition. When H_2O_2 was absent, no change occurred (Figure S3), which further provided a piece of strong evidence for our inference. To investigate the effect of H_2O_2 on the evolution of morphology, the amount of H_2O_2 was adjusted in a series of parallel experiments. As described above, the long Ag−Au−Ag NRs were formed with the addition of 150 μL of H_2O_2 (Figures 1a and 4a1,a2). When 200 μL of H_2O_2 was introduced, most products were still rodlike (Figure 4b1,b2). However, their longitudinal length decreased to 448 nm and transverse length increased to 132 nm (Figures 5 and S4c). Moreover, the inside Au decahedral NCs are close to one side of NRs along the transverse direction rather than in the central position. However, for both the starting Ag−Au−Ag NRs and long Ag−Au−Ag NRs (Figure 1), the Au decahedral NCs are in the middle along the transverse direction. The results indicate that the growth of the crystal along the transverse direction around Au decahedral NCs was isotropic, and a high concentration of H_2O_2 changed the growth preference. With further increasing H_2O_2 to 250 μL, products including dominant NRs and some nanoplates were formed (Figure 4c1,c2). The mean transverse length kept increasing to 170 nm and the longitudinal length reduced to 386 nm (Figures 5 and S4d). When 300 μL of H_2O_2 was introduced, almost all products were nanoplates and very few were NRs (Figure 4d1,d2). Their mean transverse length is 211 nm (Figures 5 and S4e). The longitudinal length had a 126 nm decrease compared with products prepared using 250 μL of H_2O_2 (Figures 5 and S4e). The composition and structure of nanoplates were investigated with elemental mapping and HRTEM. The Ag (green) and Au atom (red) distributions agree well with the HAADF result (Figure 6a−d). Elemental line scanning profiles further confirmed the structure (Figure 6e,f), demonstrating that Au decahedral NCs are located only on one side of the nanoplates.

HRTEM characterization was performed to observe the detailed structure of nanoplates (Figure 7). The nanoplate has a trapezoidal shape. The HRTEM image shows that the Au decahedron is located on one side (Figure 7a). Three regions were selected along the transverse direction. HRTEM images and corresponding FFT patterns show that they have different crystalline structures. For area 1 (Figure 7b), it is difficult to obtain a very clear lattice fringe image because of the small
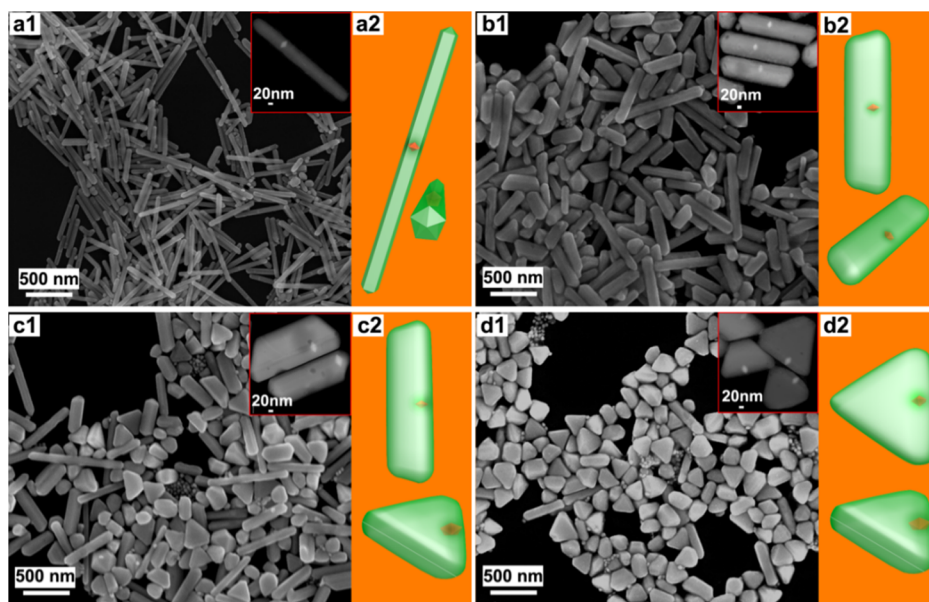
Figure 4. SEM images and corresponding schematic illustrations of products prepared through the addition of the different volumes of H_2O_2: (a1, a2) 150 μL; (b1, b2) 200 μL; (c1, c2) 250 μL; (d1, d2) 300 μL. Insets are the high-magnification HAADF images of corresponding products.
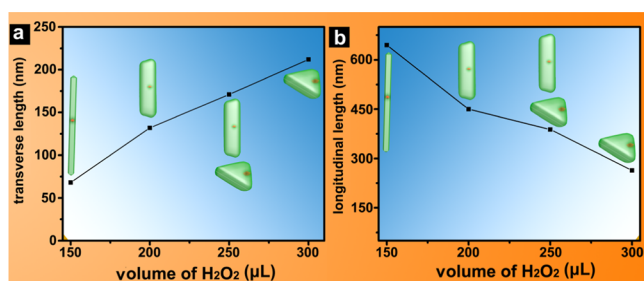

Figure 5. Transverse length (a) and longitudinal length evolution (b) as a function of the volume of H_2O_2.

spacing of the crystal plane parallel to the incident electron beam. However, it can be distinctly recognized that the spacing of adjacent crystal planes is 0.121 nm attributable to Ag(220) (Figure 7c). The corresponding FFT pattern implies that the incident electron beam was along $[\bar{1}11]$ (Figure 7d), and thus the two large bounding facets perpendicular to the incident electron beam should be Ag(111). The image contrast is inhomogeneous in area 2 because the crystalline orientation changes with positions (Figure 7e). The FFT pattern corresponding to the HRTEM image demonstrates that this area has a fivefold-twinned feature (Figure 7f), as well as the Au decahedron. Area 3 is far away from the fivefold axis and a feature similar to the single crystalline structure was observed (Figure 7g,h). Based on these TEM results, we can infer the structure of the trapezoidal nanoplate to be a combination of a single-twinned nanoplate and a fivefold-twinned NR (Figure 7i). This formation of the structure is related to two factors (the internal strain of fivefold-twinned NCs and growth kinetics) and will be discussed later.

Effect of Reaction Time. The above results show that H_2O_2 can result in a significant change in products. To gain a deep understanding of the growth, the products with different reaction times were investigated after 150 μL of H_2O_2 was added. For the products within 1 min reaction time, the products are polydispersed and a lf small-sized particles are observed (Figure 8a). We carefully removed the large-sized

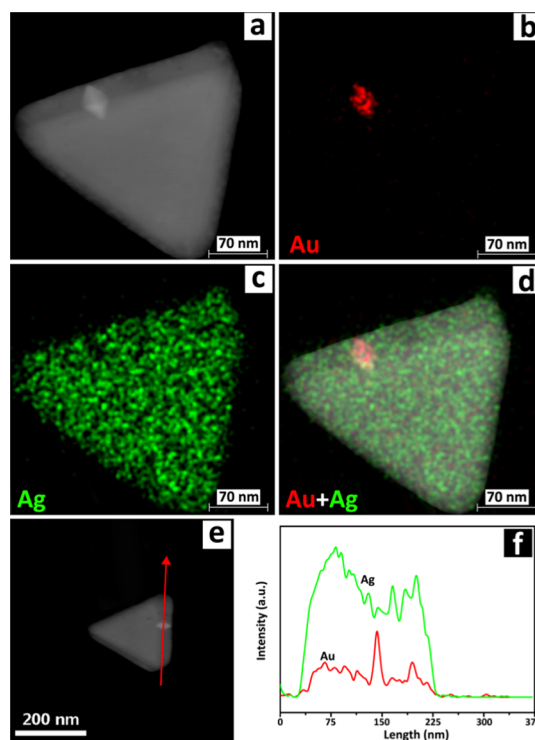**Figure 6.** HAADF images (a), elemental mapping images (b−d), and elemental line scanning profiles (e, f) of one individual triangular plate. The red arrow in (e) indicates the scanning direction.

particles through low-speed centrifugation (1500 rpm). The small-sized particles left in the solution were observed with a SEM and the result shows that they are Au decahedral NCs (inset in Figure 8a). The HRTEM image shows that Ag atoms were not etched completely (Figure S16c,d). These large-sized particles discarded in the centrifugation are Ag_2O, which is confirmed by elemental line scanning results (Figure S16a,b). If the reaction time was increased to 2 h, long NRs were observed, and the number of irregular particles reduced
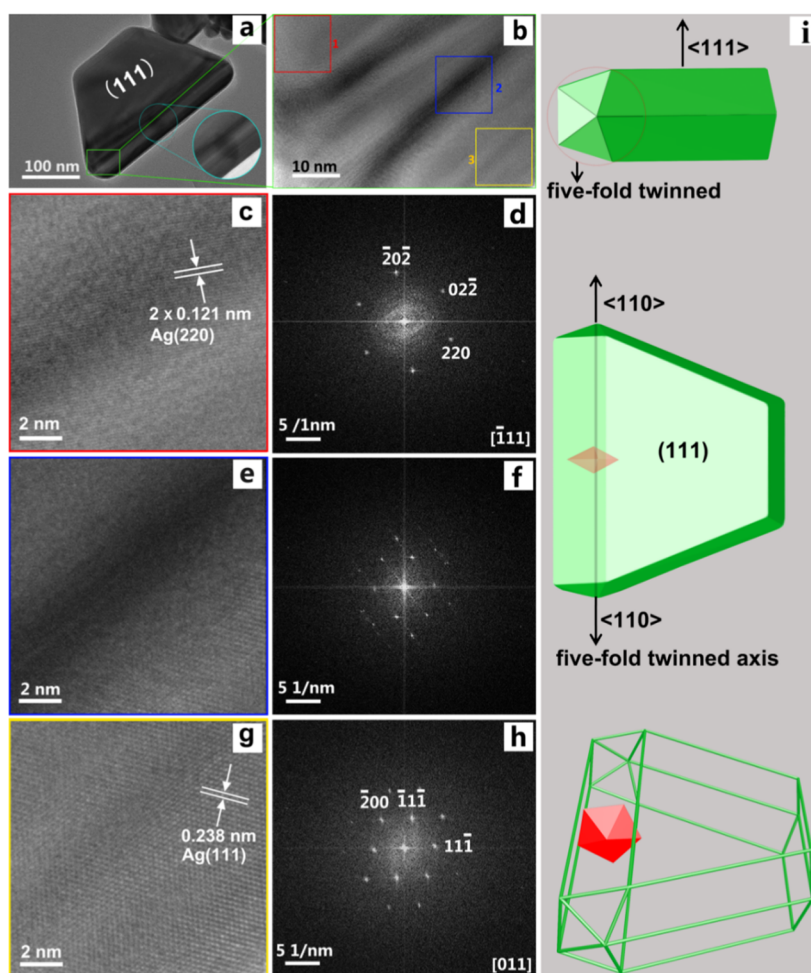
Figure 7. TEM and HRTEM images of one individual plate (a, b) and HRTEM images and corresponding fast-Fourier transform patterns of different areas: (c, d) area 1; (e, f) area 2; (g, h) area 3. The position of the Au decahedron in the nanoplate is shown by the high-magnification HRTEM image inserted in (a). (i) The top and middle figures are the schematic illustrations at different viewpoints, and the bottom figure is the perspective.

(Figure 8b). It indicated that the reduction of Ag(I) to Ag atoms occurred. The increase of the reaction time to 8 h further raised the percentage of Ag−Au−Ag NRs (Figure 8c). When the reaction was carried out for 24 h, most of the products are Ag−Au−Ag NRs (Figure 8d). In the current case, almost no irregular particles were observed, implying that Ag(I) was consumed almost completely. It is necessary to mention that in the experiment, no additional Ag precursor was introduced and the formation of large-sized Ag−Au bimetallic NCs indicates that only a small amount of Au decahedral NCs served as nucleation centers in the Ag regrowth. A large number of separate Au decahedral NCs were observed after the regrowth. Due to the large size difference, Ag−Ag NCs can be separated easily from Au decahedral NCs via precipitation to gain products with a uniform shape (Figure 1b).

Growth Mechanism. Based on the time-dependent evolution, we may conclude that the reconstruction includes two stages. In the first stage, Ag atoms of the Ag−Au−Ag NRs transform to Ag(I) due to the etching of H_2O_2 and Au decahedral NCs remained due to their high stability. In the second stage, Ag(I) is reduced back to Ag atoms, which nucleate again on some Au decahedral NC surfaces along ⟨110⟩ and form Ag−Au−Ag NRs. For the first stage, it can be

easily understood because H_2O_2 is a strong oxidant. Many publications also reported the etching of Ag by H_2O_2.[33−35] Herein, two critical questions in the second stage are worth discussing.

The first question is which substances act as reducing agents. As discussed before, H_2O_2 can also serve as a reductant in some cases, especially when it is in an alkaline environment.[33−35,40] Ekgasit et al. demonstrated that H_2O_2 could trigger the shape transformation from Ag nanospheres to Ag nanoplates.[33,34] They believed that H_2O_2 first etched Ag and then reduced Ag ions, resulting in the regeneration of Ag nanoplates. In another report, Yin and co-workers systematically studied the H_2O_2-assisted growth of Ag nanoplates and deepened the understanding that Ag(I) is reduced to Ag by HO_2^- anions rather than H_2O_2.[35] Our system could partially be explained by the same mechanism but there are some differences. In their systems, various organic substances were used to stabilize nanoplates or guide crystal growth. In our experiment, no organic substances were introduced in the second stage. Moreover, the Ag−Au−Ag NRs were washed at least three times to remove excess PDDA, DEG, and other by-products. After Ag was oxidized by H_2O_2, Ag_2O rather than other Ag(I) complexes was formed because no other ions were present. Ag_2O is a non-water-soluble substance. After Ag atoms
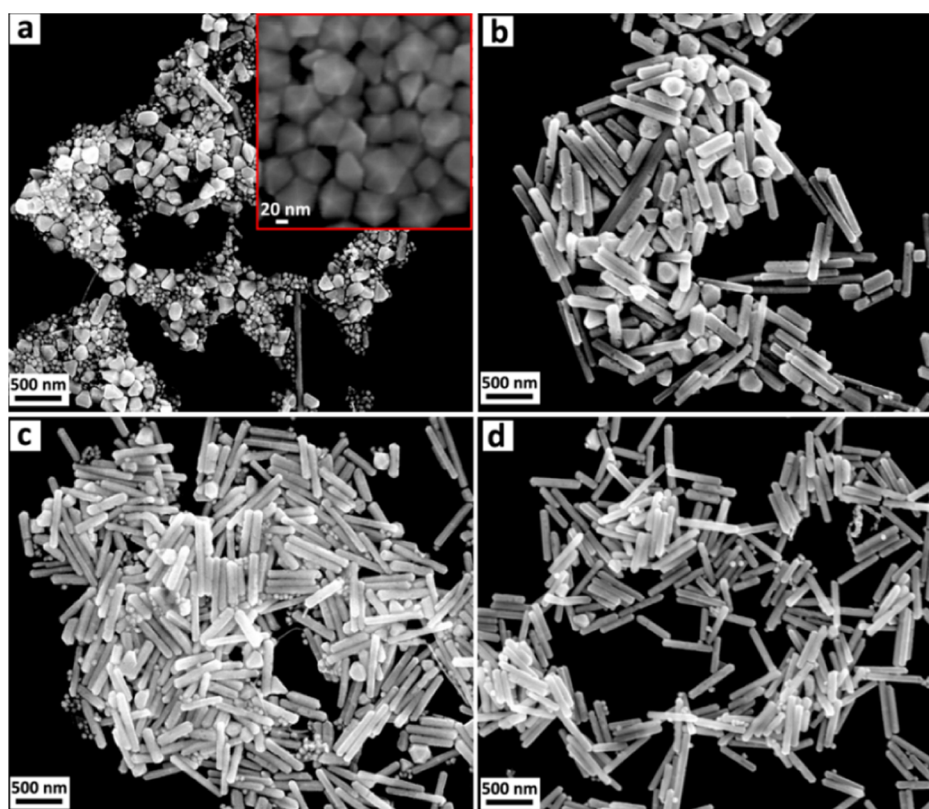
Figure 8. SEM images of products prepared through adjusting the reaction time (150 μL of H_2O_2 was added): (a) 1 min; (b) 2 h; (c) 8 h; and (d) 24 h. The inset in (a) is the SEM image of products after removing the large-sized particles, showing the remaining Au decahedral NCs.

Scheme 1. (a) Top View of Decahedral Geometry along ⟨110⟩; (b) Schematic Illustration of Transverse Growth and Longitudinal Growth; (c) Nanocrystal Formation and Evolution with the Reduction Rate
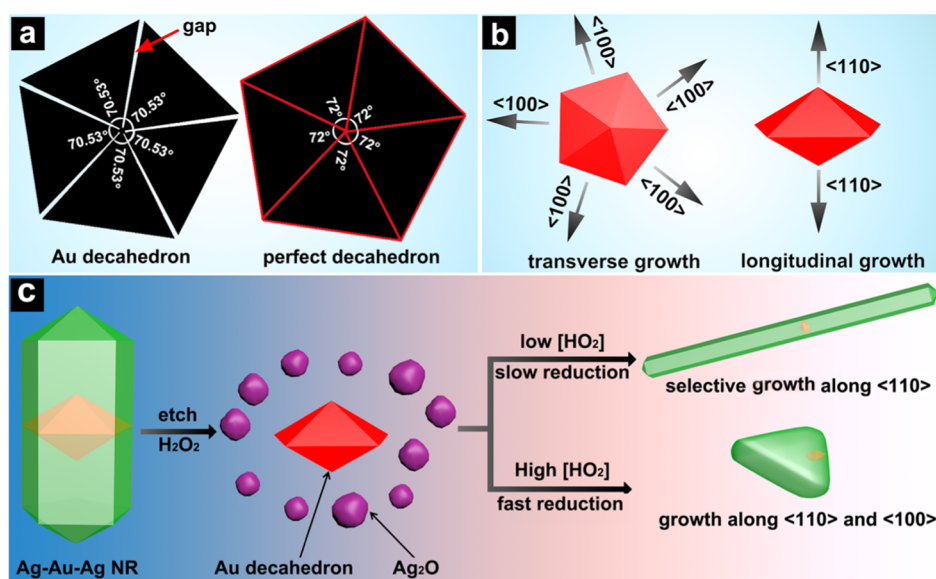
on the surface are oxidized, the Ag_2O layer can prevent further etching. Ultrasonic treatment in our experiment can remove the Ag_2O layer from the Ag–Au–Ag surface. As a result, further etching may occur. Otherwise, length and shape changes were not that fast. An alkaline environment can produce high-concentration HO_2^- anions and then provide H_2O_2 with a stronger reducing ability. In our experiment, no alkaline substance was used, and the solution was acidic (pH = 4.7). However, the reduction of Ag(I) to Ag atoms still

occurred. Therefore, the formation of Ag_2O is an important step. The standard redox potential of Ag_2O/Ag is 1.17 V, which is higher than those the other redox pairs ($E(AgCl/Ag)$ = 0.222 V; $E(AgBr/Ag)$ = 0.0713 V; $E(Ag^+/Ag)$ = 0.7996 V).[41] The high standard redox potential facilitates the reduction. To confirm this, we introduced 10 μL of PDDA containing Cl^- ions and other conditions were unchanged. On coming in contact with Cl^-, Ag_2O can change into AgCl owing to its stability difference.[42] In this case, Ag should transform

into AgCl instead of Ag$_2$O after etching. The result showed that only etching was observed, and the regrowth of Ag did not occur because the formation of AgCl provided an energy barrier to reduce Ag(I) to Ag atoms (Figures S10 and S11).

Another critical question is how Au decahedral NCs and the amount of H$_2$O$_2$ affect the product shape. For a perfect decahedron with fivefold symmetry, the angle between two adjacent subunits should be 72° (Scheme 1a).[36−38,43−46] However, the angle between two adjacent subunits in a fivefold-twined Au decahedron and its derivative NR is only 70.53°, which causes a 7.35° solid-angle deficiency.[47,48] To connect each subunit, the lattices near twinned boundaries have to be stretched. As a result, the NCs are intrinsically strained. Moreover, the gap between two adjacent subunits increases with the transverse length, and so does the strain. Therefore, the internal strain always restricts the transverse growth and favors the longitudinal growth along ⟨110⟩ (Scheme 1b).[42] That is, the product with a large transverse length is not promoted thermodynamically in the fivefold-twinned NCs.

In our experiment, H$_2$O$_2$ can be divided into three parts. Part I and part II are consumed in the etching of Ag and the reduction of Ag$_2$O to Ag(0), respectively. Part III is the extra H$_2$O$_2$ that is not involved in the etching and reduction. Although part III does not participate in the above two chemical reactions, it is critical to the etching and reduction rate. When Ag concentration is kept unchanged, the amounts consumed in etching and reduction are constant. The total H$_2$O$_2$ concentration depends on part III, determines the collision frequency between the reactants, and affects etching and reduction rate kinetically. With increasing H$_2$O$_2$, etching and the kinetics of reduction increase.

Growth kinetics can significantly affect the growth mode and product shape, as well as intrinsic strain.[20,49,50] Slow reduction causes low-concentration Ag atoms. As a result, after the newly formed Ag atoms adsorb on the Au decahedral NC surface, they can migrate to thermodynamically favorable sites for reaching a low-energy state. As discussed above, a large transverse length is a high-energy state. Consequently, the growth along ⟨110⟩ is promoted, forming Ag−Au−Ag NRs with a large aspect ratio (Scheme 1c). For a fast reduction, high-concentration Ag atoms are generated. In this case, Ag atoms prefer nucleating on these positions where they first adsorb. For this reason, transverse growth is accelerated and longitudinal growth relatively slows down (Scheme 1c), which is unfavorable due to increased strain. It has been demonstrated that asymmetrical transverse growth can alleviate the strain.[43,45] Therefore, transverse growth mainly occurred along one side, generating nanoplates in which Au decahedral NC seeds are not located in the middle rather on one side (Scheme 1c).

Effect of Ag Precursor Concentration. The kinetics dependent growth mode can be demonstrated again by controlling other reaction conditions. We designed a series of experiments in which 300 μL of H$_2$O$_2$ was fixed and different amounts of pure Ag NCs were added (Figures S12−S14). As a result of more Ag atoms, the amount of H$_2$O$_2$ consumed in the etching increased, and so the concentration of H$_2$O$_2$ in the next reduction became low, resulting in a slow reduction. Under this circumstance, the transverse growth rate should decrease and transverse length must have the same change. Results show that the products indeed evolved from the plate with a large transverse length to high aspect ratio NRs

with the introduction of Ag NCs. Previously, Parnklang et al. reported that only starting Ag nanospheres smaller than 10 nm could induce the regeneration of Ag atoms because the small size effect causes high reactivity and collision frequency.[33] Otherwise, only etching was observed and Ag(I) could not be reduced back to Ag atoms. In our system, the size of starting Ag NCs and Ag−Au−Ag NRs are far larger than 10 nm (Figure S12), and so there is no such size limit in our system. This could be attributed to the high redox potential of Ag$_2$O, which makes the reduction of Ag(I) to Ag easier.

SERS Measurement. When Ag NCs or Au NCs are irradiated by light, the electric field near their surface can be heavily enhanced due to localized surface plasmon resonance absorption. For this reason, the polarizability of the Raman probe molecule on Ag or Au substrates has a very strong increase, producing a strong Raman intensity. Therefore, they are widely used as SERS substrates and their surface morphology significantly affects SERS performance.[51,52] High-resolution SEM images show that the starting Ag−Au−Ag NRs have relatively smooth surfaces (Figure 9a), but the
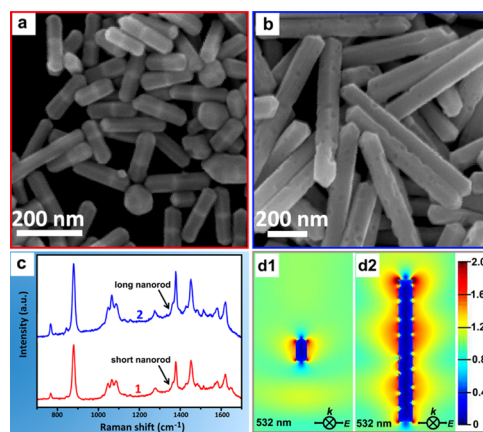

Figure 9. SEM images of short Ag−Au−Ag NRs (a), long Ag−Au−Ag NRs (b), their SERS spectra (c), and corresponding FDTD simulations of the electric field on the NC surface (d1, d2).

prepared long NRs have a large number of pinholes on their surface (Figure 9b). This could be caused by the concentration difference of capping agents during their growth. The concentration of capping agents was much lower in the preparation of long NRs, and thereby the crystal growth was not well guided, which might result in the formation of defects (pinholes). It has been demonstrated that the pinhole effect on Au or Ag NC surfaces can generate a considerable enhancement of the electromagnetic field, which greatly improves their SERS performance.[53−55] Here, the SERS performance of the two NRs were tested, and both of them give clear enhanced Raman spectra using 2-naphthalenethiol as the probe molecules. However, 2-naphthalenethiol ethanol solution without metal nanoparticles could only produce a very weak Raman signal even when the concentration is 1 M (Figure S19), demonstrating that both bimetallic NRs have excellent SERS performance. For the SERS tests of the two bimetallic NRs, the Ag content is constant. However, the size of the latter is larger than that of the former. Theoretically, the total surface area of short NRs should be higher and result in a better SERS performance. However, the SERS performance of long Ag−Ag−Ag NRs is 1.4 times of that recorded on the short NRs (Figure 9c). Here, the better SERS performance of

reconstructed long Ag−Au−Ag NRs can result from the pinhole effect. We also calculated the enhancement factor (Figures S17−S20 and Table S1). Although reconstructed Ag−Au−Ag NRs have a smaller surface area and absorb less probe molecules than original Ag−Au−Ag NRs, the former has a higher enhancement factor (9.0×10^5), which is 2.5 times that of the latter (3.6×10^5). To confirm the pinhole effect, we performed a finite-difference time-domain (FDTD) simulation. When the source (532 nm) was injected along the longitudinal direction, the electromagnetic field near each pinhole has an enhancement clearly (Figure 9d1,d2), implying that surface pinholes provide numerous hot spots. Therefore, the Raman signal is dramatically enhanced. The surface plasmon resonance absorption along the transverse direction could also result in the SERS enhancement. For Ag NRs with diameters ranging from 50 to 90 nm, the surface plasmon resonance absorption often appears at 450 nm,[56,57] but the wavelength of the used laser in our experiment is 532 nm. Therefore, the SERS enhancement should be due to the pinhole effect rather than the excitation of the laser.

CONCLUSIONS

We have demonstrated that the two-stage reconstruction (etching and regrowth) of fivefold-twinned Ag−Au−Ag NRs is achieved with H_2O_2 both as an oxidant and a reductant. Products with various shapes and structures can be prepared by tuning the concentration of H_2O_2 and other conditions. The internal strain of the fivefold-twinned structure has a critical effect on the product morphology for it can restrict the transverse growth and relatively facilitate the growth along the $\langle 110 \rangle$ direction. That is, it favors the formation of NRs with a high aspect ratio. Growth kinetics also has decisive impacts. Slow growth has the same effect as the internal strain. However, fast growth prefers asymmetrical transverse growth and the formation of nanoplates. The surface of reconstructed Ag−Au−Ag NRs has abundant pinholes, which can enhance the electromagnetic field and improve SERS performance when they serve as substrates. It is believed that our studies can considerably expand the utilization of H_2O_2 in the controlled preparation of Ag NCs and practical applications.

ASSOCIATED CONTENT

Ⓢ Supporting Information

The Supporting Information is available free of charge at https://pubs.acs.org/doi/10.1021/acs.langmuir.0c01230.

Other results (TEM, SEM, elemental line scanning, elemental mapping, and size distribution), FDTD simulations, and the synthetic method of Ag NCs (PDF)

AUTHOR INFORMATION

Corresponding Authors

Haihong Wen − *College of Life and Environmental Science, Wenzhou University, Wenzhou 325035, China*; Email: whh@wzu.edu.cn

Wei Wang − *Department of Chemistry & Center for Pharmacy, University of Bergen, 5020 Bergen, Norway*; ⓞ orcid.org/0000-0001-6777-2441; Email: wei.wang@uib.no

Yun Yang − *Nanomaterials and Chemistry Key Laboratory, Wenzhou University, Wenzhou 325035, China*; ⓞ orcid.org/0000-0002-8661-7444; Email: bachier@163.com

Authors

Hui Hao − *Nanomaterials and Chemistry Key Laboratory, Wenzhou University, Wenzhou 325035, China*

Yinliang Yang − *College of Pharmacy, Liaocheng University, Liaocheng 252000, Shandong, China*

Chao Zou − *Nanomaterials and Chemistry Key Laboratory, Wenzhou University, Wenzhou 325035, China*

Wei Chen − *Nanomaterials and Chemistry Key Laboratory, Wenzhou University, Wenzhou 325035, China*

Complete contact information is available at:
https://pubs.acs.org/10.1021/acs.langmuir.0c01230

Notes

The authors declare no competing financial interest.

REFERENCES

(1) Zhang, Z. C.; Liu, G. G.; Cui, X. Y.; Chen, B.; Zhu, Y. H.; Gong, Y.; Saleem, F.; Xi, S. B.; Du, Y. H.; Borgna, A.; Lai, Z. C.; Zhang, Q. H.; Li, B.; Zong, Y.; Han, Y.; Gu, L.; Zhang, H. Crystal Phase, and Architecture Engineering of Lotus-Thalamus-Shaped Pt-Ni Anisotropic Superstructures for Highly Efficient Electrochemical Hydrogen Evolution. *Adv. Mater.* **2018**, *30*, No. 1801741.

(2) Wang, J.; Zhang, W.; Li, S.; Miao, D.; Qian, G.; Su, G. Engineering of Porous Silica Coated Gold Nanorods by Surface-Protected Etching and Their Applications in Drug Loading and Combined Cancer Therapy. *Langmuir* **2019**, *35*, 14238−14247.

(3) Sun, Y.; Li, T. Composition-Tunable Hollow Au/Ag SERS Nanoprobes Coupled with Target-Catalyzed Hairpin Assembly for Triple-Amplification Detection of miRNA. *Anal. Chem.* **2018**, *90*, 11614−11621.

(4) Huo, D.; Kim, M. J.; Lyu, Z.; Shi, Y.; Wiley, B. J.; Xia, Y. One-Dimensional Metal Nanostructures: From Colloidal Syntheses to Applications. *Chem. Rev.* **2019**, *119*, 8972−9073.

(5) Li, Y.; Yu, H.; Wang, Z.; Liu, S.; Xu, Y.; Li, X.; Wang, L.; Wang, H. Boron-Doped Silver Nanosponges with Enhanced Performance towards Electrocatalytic Nitrogen Reduction to Ammonia. *Chem. Commun.* **2019**, 14745−14748.

(6) Kang, X.; Ruan, Q.; Zhang, H.; Bao, F.; Guo, J.; Tang, M.; Cheng, S.; Wang, J. Concave Gold Bipyramids Bound with Multiple High-Index Facets: Improved Raman and Catalytic Activities. *Nanoscale* **2017**, *9*, 5879−5886.

(7) González-Rubio, G.; González-Izquierdo, J.; Bañares, L.; Tardajos, G.; Rivera, A.; Altantzis, T.; Bals, S.; Peña-Rodríguez, O.; Guerrero-Martínez, A.; Liz-Marzán, L. M. Femtosecond Laser-Controlled Tip-to-Tip Assembly and Welding of Gold Nanorods. *Nano Lett.* **2015**, *15*, 8282−8288.

(8) Chen, H. J.; Shao, L.; Li, Q.; Wang, J. F. Gold Nanorods and Their Plasmonic Properties. *Chem. Soc. Rev.* **2013**, *42*, 2679−2724.

(9) Gilroy, K. D.; Ruditskiy, A.; Peng, H.-C.; Qin, D.; Xia, Y. N. Bimetallic Nanocrystals: Syntheses, Properties, and Applications. *Chem. Rev.* **2016**, *116*, 10414−10472.

(10) Niu, W.; Liu, J.; Huang, J.; Chen, B.; He, Q.; Wang, A.-L.; Lu, Q.; Chen, Y.; Yun, Q.; Wang, J.; Li, C.; Huang, Y.; Lai, Z.; Fan, Z.; Wu, X.-J.; Zhang, H. Unusual 4H-Phase Twinned Noble Metal Nanokites. *Nat. Commun.* **2019**, *10*, No. 2881.

(11) Jiang, X.; Qiu, X.; Fu, G.; Sun, J.; Huang, Z.; Sun, D.; Xu, L.; Zhou, J.; Tang, Y. Highly Simple and Rapid Synthesis of Ultrathin Gold Nanowires with (111)-Dominant Facets and Enhanced Electrocatalytic Properties. *J. Mater. Chem. A* **2018**, *6*, 17682−17687.

(12) Chen, D.; Wang, Y.; Liu, D.; Li, H.; Qian, C.; He, H.; Yang, J. Surface Composition Dominates the Electrocatalytic Reduction of CO2 on Ultrafine CuPd Nanoalloys. *Carbon Energy* **2020**, 1−9.

(13) Jiang, T.; Chen, G.; Tian, X.; Tang, S.; Zhou, J.; Feng, Y.; Chen, H. Construction of Long Narrow Gaps in Ag Nanoplates. *J. Am. Chem. Soc.* **2018**, *140*, 15560−15563.

(14) Zhang, W.; Liu, J.; Niu, W.; Yan, H.; Lu, X.; Liu, B. Tip-Selective Growth of Silver on Gold Nanostars for Surface-Enhanced Raman Scattering. *ACS Appl. Mater. Interfaces* **2018**, *10*, 14850−14856.

(15) Fang, C.; Zhao, J.; Jiang, R.; Wang, J.; Zhao, G.; Geng, B. Engineering of Hollow PdPt Nanocrystals via Reduction Kinetic Control for Their Superior Electrocatalytic Performances. *ACS Appl. Mater. Interfaces* **2018**, *10*, 29543−29551.

(16) Li, F.; Shao, Q.; Hu, M.; Chen, Y.; Huang, X. Hollow Pd-Sn Nanocrystals for Efficient Direct H₂O₂ Synthesis: the Critical Role of Sn on Structure Evolution and Catalytic Performance. *ACS Catal.* **2018**, *8*, 3418−3423.

(17) Crane, C. C.; Tao, J.; Wang, F.; Zhu, Y.; Chen, J. Mask-Assisted Seeded Growth of Segmented Metallic Heteronanostructures. *J. Phys. Chem. C* **2014**, *118*, 28134−28142.

(18) Smith, J. D.; Woessner, Z. J.; Skrabalak, S. E. Branched Plasmonic Nanoparticles with High Symmetry. *J. Phys. Chem. C* **2019**, *123*, 18113−18123.

(19) Qiu, J.; Camargo, P. H. C.; Jeong, U.; Xia, Y. N. Synthesis, Transformation, and Utilization of Monodispersed Colloidal Spheres. *Acc. Chem. Res.* **2019**, *52*, 3475−3487.

(20) Wang, Y.; He, J.; Liu, C.; Chong, W. H.; Chen, H. Thermodynamics versus Kinetics in Nanosynthesis. *Angew. Chem., Int. Ed.* **2015**, *54*, 2022−2051.

(21) Bian, T.; Zhang, H.; Jiang, Y.; Jin, C.; Wu, J.; Yang, H.; Yang, D. Epitaxial Growth of Twinned Au-Pt Core-Shell Star-Shaped Decahedra as Highly Durable Electrocatalysts. *Nano Lett.* **2015**, *15*, 7808−7815.

(22) Liu, H.; Liu, K.; Zhong, P.; Qi, J.; Bian, J.; Fan, Q.; Ren, K.; Zheng, H.; Han, L.; Yin, Y.; Gao, C. Ultrathin Pt−Ag Alloy Nanotubes with Regular Nanopores for Enhanced Electrocatalytic Activity. *Chem. Mater.* **2018**, *30*, 7744−7751.

(23) Wang, W.; Li, W.; He, T.; Liu, Y.; Jin, M. Engineering Surface Structure of Pt Nanoshells on Pd Nanocubes to Preferentially Expose Active Surfaces for ORR by Manipulating the Growth Kinetics. *Nano Lett.* **2019**, *19*, 1743−1748.

(24) Chen, Q.; Jia, Y.; Xie, S.; Xie, Z. Well-Faceted Noble-Metal Nanocrystals with Nonconvex Polyhedral Shapes. *Chem. Soc. Rev.* **2016**, *45*, 3207−3220.

(25) Nosheen, F.; Zhang, Z.; Xiang, G.; Xu, B.; Yang, Y.; Saleem, F.; Xu, X.; Zhang, J.; Wang, X. Three-Dimensional Hierarchical Pt-Cu Superstructures. *Nano Res.* **2015**, *8*, 832−838.

(26) Daniel, J. R.; McCarthy, L. A.; Yazdi, S.; Chagnot, M.; Ringe, E.; Boudreau, D. Gold Speciation and Co-Reduction Control the Morphology of AgAu Nanoshells in Formaldehyde-Assisted Galvanic Replacement. *J. Phys. Chem. C* **2018**, *122*, 18168−18176.

(27) Lindley, S. A.; Cooper, J. K.; Rojas-Andrade, M. D.; Fung, V.; Leahy, C. J.; Chen, S.; Zhang, J. Z. Highly Tunable Hollow Gold Nanospheres: Gaining Size Control and Uniform Galvanic Exchange of Sacrificial Cobalt Boride Scaffolds. *ACS Appl. Mater. Interfaces* **2018**, *10*, 12992−13001.

(28) Ahn, J.; Qin, D. Fabrication of Nanoscale Cage Cubes by Drilling Orthogonal, Intersected Holes through All Six Side Faces of Ag Nanocubes. *Chem. Mater.* **2019**, *31*, 9179−9187.

(29) Zhao, M.; Hood, Z. D.; Vara, M.; Gilroy, K. D.; Chi, M.; Xia, Y. Ruthenium Nanoframes in the Face-Centered Cubic Phase: Facile Synthesis and Their Enhanced Catalytic Performance. *ACS Nano* **2019**, *13*, 7241−7251.

(30) Zhu, X.; Xu, J.; Zhang, H.; Cui, X.; Guo, Y.; Cheng, S.; Kan, C.; Wang, J. Gold Nanobipyramid-Embedded Ultrathin Metal Nanoframes for In Situ Monitoring Catalytic Reactions. *Chem. Sci.* **2020**, *11*, 3198−3207.

(31) Mulvihill, M.; Ling, X.; Henzie, J.; Yang, P. Anisotropic Etching of Silver Nanoparticles for Plasmonic Structures Capable of Single-Particle SERS. *J. Am. Chem. Soc.* **2010**, *132*, 268−274.

(32) Zhou, S.; Huo, D.; Goines, S.; Yang, T.-H.; Lyu, Z.; Zhao, M.; Gilroy, K. D.; Wu, Y.; Hood, Z. D.; Xie, M. Enabling Complete Ligand Exchange on the Surface of Gold Nanocrystals through the Deposition and Then Etching of Silver. *J. Am. Chem. Soc.* **2018**, *140*, 11898−11901.

(33) Parnklang, T.; Lertvachirapaiboon, C.; Pienpinijtham, P.; Wongravee, K.; Thammacharoen, C.; Ekgasit, S. H₂O₂-Triggered Shape Transformation of Silver Nanospheres to Nanoprisms with Controllable Longitudinal Lspr Wavelengths. *RSC Adv.* **2013**, *3*, 12886−12894.

(34) Parnklang, T.; Lamlua, B.; Gatemala, H.; Thammacharoen, C.; Kuimalee, S.; Lohwongwatana, B.; Ekgasit, S. Shape Transformation of Silver Nanospheres to Silver Nanoplates Induced by Redox Reaction of Hydrogen Peroxide. *Mater. Chem. Phys.* **2015**, *153*, 127−134.

(35) Yu, H.; Zhang, Q.; Liu, H.; Dahl, M.; Joo, J. B.; Li, N.; Wang, L.; Yin, Y. Thermal Synthesis of Silver Nanoplates Revisited: A Modified Photochemical Process. *ACS Nano* **2014**, *8*, 10252−10261.

(36) Li, X.; Yang, Y.; Zhou, G.; Han, S.; Wang, W.; Zhang, L.; Chen, W.; Zou, C.; Huang, S. The Unusual Effect of AgNO₃ on the Growth of Au Nanostructures and their Catalytic Performance. *Nanoscale* **2013**, *5*, 4976−4985.

(37) Yang, Y.; Wang, W.; Li, X.; Chen, W.; Fan, N.; Zou, C.; Chen, X.; Xu, X.; Zhang, L.; Huang, S. Controlled Growth of Ag/Au Bimetallic Nanorods through Kinetics Control. *Chem. Mater.* **2013**, *25*, 34−41.

(38) Luo, M.; Huang, H.; Choi, S.-I.; Zhang, C.; da Silva, R. R.; Peng, H.-C.; Li, Z.-Y.; Liu, J.; He, Z.; Xia, Y. Facile Synthesis of Ag Nanorods with No Plasmon Resonance Peak in the Visible Region by Using Pd Decahedra of 16 nm in Size as Seeds. *ACS Nano* **2015**, *9*, 10523−10532.

(39) Ni, C.; Hassan, P. A.; Kaler, E. W. Structural Characteristics and Growth of Pentagonal Silver Nanorods Prepared by a Surfactant Method. *Langmuir* **2005**, *21*, 3334−3337.

(40) Nishimoto, M.; Abe, S.; Yonezawa, T. New Preparation of Ag Nanoparticles Using Hydrogen Peroxide as a Reducing Agent. *New J. Chem.* **2018**, *42*, 14493−14501.

(41) Lide, D. R., Ed. *CRC Handbook of Chemistry and Physics*; Electrochemical Series, Internet version 2005; CRC Press: Boca Raton, FL, 2005. http://www.hbcpnetbase.com.

(42) Yang, S.; Xu, D.; Chen, B.; Luo, B.; Shi, W. In-Situ Synthesis of a Plasmonic Ag/AgCl/Ag2O Heterostructures for Degradation of Ciprofloxacin. *Appl. Catal., B* **2017**, *204*, 602−610.

(43) Zhang, W. J.; Liu, Y.; Cao, R. G.; Li, Z. H.; Zhang, Y. H.; Tang, Y.; Fan, K. N. Synergy between Crystal Strain and Surface Energy in Morphological Evolution of Five-Fold-Twinned Silver Crystals. *J. Am. Chem. Soc.* **2008**, *130*, 15581−15588.

(44) Song, M.; Wu, Z.; Lu, N.; Li, D. Strain Relaxation-Induced Twin Interface Migration and Morphology Evolution of Silver Nanoparticles. *Chem. Mater.* **2019**, *31*, 842−850.

(45) Jin, B.; Sushko, M. L.; Liu, Z.; Cao, X.; Jin, C.; Tang, R. Understanding Anisotropic Growth of Au Penta-Twinned Nanorods by Liquid Cell Transmission Electron Microscopy. *J. Phys. Chem. Lett.* **2019**, *10*, 1443−1449.

(46) Huang, X.; Zheng, N. One-Pot, High-Yield Synthesis of 5-Fold Twinned Pd Nanowires and Nanorods. *J. Am. Chem. Soc.* **2009**, *131*, 4602−4603.

(47) Casillas, G.; Velázquez-Salazar, J. J.; Jose-Yacaman, M. A New Mechanism of Stabilization of Large Decahedral Nanoparticles. *J. Phys. Chem. C* **2012**, *116*, 8844−8848.

(48) Johnson, C. L.; Snoeck, E.; Ezcurdia, M.; Rodríguez-González, B.; Pastoriza-Santos, I.; Liz-Marzán, L. M.; Hÿtch, M. J. Effects of Elastic Anisotropy on Strain Distributions in Decahedral Gold Nanoparticles. *Nat. Mater.* **2008**, *7*, 120−124.

(49) Qi, X.; Chen, Z.; Yan, T.; Fichthorn, K. A. Growth Mechanism of Five-Fold Twinned Ag Nanowires from Multiscale Theory and Simulations. *ACS Nano* **2019**, *13*, 4647−4656.

(50) Gilroy, K. D.; Hughes, R. A.; Neretina, S. Kinetically Controlled Nucleation of Silver on Surfactant-Free Gold Seeds. *J. Am. Chem. Soc.* **2014**, *136*, 15337−15345.

(51) Gilroy, K. D.; Peng, H.-C.; Yang, X.; Ruditskiy, A.; Xia, Y. N. Symmetry Breaking during Nanocrystal Growth. *Chem. Commun.* **2017**, *53*, 4530−4541.

(52) Uzayisenga, V.; Lin, X. D.; Li, L. M.; Anema, J. R.; Yang, Z. L.; Huang, Y. F.; Lin, H. X.; Li, S. B.; Li, J. F.; Tian, Z. Q. Synthesis, Characterization, and 3D-FDTD Simulation of Ag@SiO$_2$ Nanoparticles for Shell-Isolated Nanoparticle-Enhanced Raman Spectroscopy. *Langmuir* **2012**, *28*, 9140−9146.

(53) Dai, L.; Song, L.; Huang, Y.; Zhang, L.; Lu, X.; Zhang, J.; Chen, T. Bimetallic Au Ag Core-Shell Superstructures with Tunable Surface Plasmon Resonance in the Near-Infrared Region and High Performance Surface-Enhanced Raman Scattering. *Langmuir* **2017**, *33*, 5378−5384.

(54) Hao, E.; Li, S. Y.; Bailey, R. C.; Zou, S. L.; Schatz, G. C.; Hupp, J. T. Optical Properties of Metal Nanoshells. *J. Phys. Chem. B* **2004**, *108*, 1224−1229.

(55) Han, S.-Y.; Guo, Q.-H.; Xu, M.-M.; Yuan, Y.-X.; Shen, L.-M.; Yao, J.-L.; Liu, W.; Gu, R.-A. Tunable Fabrication on Iron Oxide/Au/Ag Nanostructures for Surface Enhanced Raman Spectroscopy and Magnetic Enrichment. *J. Colloid Interface Sci.* **2012**, *378*, 51−57.

(56) Zhao, Y. P.; Chaney, S. B.; Zhang, Z. Y. Absorbance spectra of aligned Ag nanorod arrays prepared by oblique angle deposition. *J. Appl. Phys.* **2006**, *100*, No. 063527.

(57) Zhang, J.; Langille, M. R.; Mirkin, C. A. Synthesis of Silver Nanorods by Low Energy Excitation of Spherical Plasmonic Seeds. *Nano Lett.* **2011**, *11*, 2495−2498.